# An Analysis of the Sixteen-Blade Aircraft Engine Cooling Fan using Computational Fluid Dynamics

**KAVALI SHIVAKUMAR[1], Dr. K. SAMMAIAH[2], Dr.B. SANDHYA RANI[3]**

*[1]PG Student, CAD/CAM, Ellenki College of Engineering and Technology.*

*[2]Assoc Prof., Department of Mechanical Engineering, Ellenki College of Engineering and Technology.*

*[3]Head of the Dept. Department of Mechanical Engineering, Ellenki College of Engineering and Technology.*

**Abstract -** When running on the ground, taxiing, taking off, or flying at low speeds, the airflow across the cylinder fins, oil cooler, and accessory case isn't enough to cool the pistons and turbines of an air-cooled aircraft. This is especially true for rotorcraft that hover for long periods of time. Consequently, a specialized axial cooling fan is often used in these setups. The thermal margin of the whole engine installation is determined by its pressure-flow characteristic, which is the static pressure increase it can withstand at a given rotational speed and volumetric flow. A sixteen-blade axial engine cooling fan with a spinner, hub, and a row of blades with a circular pattern is described in this work, along with its computational fluid dynamics analysis and solid modeling. A single blade profile was arranged around the hub axis at 22.5° spacing using the Circular Pattern function in CATIA V5's Sketcher and Part Design workbenches to model the rotor. The finished geometry was then imported into ANSYS Workbench and solved using the Fluid Flow (CFX) system. Separated by a fluid-fluid interface, the fluid domain was discretized into a combined tetrahedral mesh of 25,163 nodes and 133,334 elements, with the inner area including the spinner and hub and the outer region containing the blades and the surrounding flow field. With no-slip walls, an average static pressure at the outlet, and an input velocity of 65 m/s, a stationary-frame, steady-state, laminar solution was found for air. In spite of falling short of the nominal $1 \times 10^{-4}$ objective, the solver achieved its 100-iteration limit with RMS residuals plateauing between around $7 \times 10^{-4}$ and $2.6 \times 10^{-3}$. Normalized mass and momentum imbalances stayed below 0.04% throughout, suggesting a rather cautious solution that has not completely converged. The resultant flow pattern displayed a static-pressure gradient across the fan ranging from about -7.18 kPa to +5.58 kPa, with local velocities reaching 110 m/s close to the blade tips. Over and above the corresponding viscous force and moment components, there was a dominant axial pressure force of about 476 N and an axial pressure moment of about -143.5 N·m. Along with the CATIA geometry, these findings define the pressure increase and axial thrust supplied by the fan under the simulated situation. They also serve as a foundation for future structural, turbulence-resolved, and rotating-frame analyses of the cooling-fan assembly. In order to improve the accuracy of the analysis, we point out the shortcomings in the mesh quality, the solver convergence, and the assumptions made about the flow regime, and we suggest specific solutions.

**Terms for Index —** Engine heat management, computational fluid dynamics, axial fans, pressure rise, and aircraft engines, as well as CATIA V5 and ANSYS CFX.

## I. INTRODUCTION

The majority of the chemical energy released during combustion is lost as heat in the exhaust, engine structure, lubricating oil, and accessory components. To ensure operational safety, material strength, and reliability, it is crucial to keep this heat load within safe limits, as aircraft piston and gas-turbine engines only convert a fraction of this energy into usable work, usually 25-40% [1, 2]. There is little extra power consumption during cruise flight because the ram air that enters the cowl inlets is spread across the cylinder fins and oil cooler by internal baffles. Although engine power and heat generation may be high, rotorcraft face this issue most acutely during ground operation, taxi, take-off, initial climb, and low-speed manoeuvring due to the lack of forward airspeed and, by extension, the ram-air pressure differential, which prevents sufficient cooling flow [2, 3].

In order to maintain enough airflow even while the aircraft is moving at high speeds, many engines include a separate cooling fan that is either powered by electricity or driven by the engine's belt, gear, or shaft. From an aerodynamic perspective, this type of fan functions similarly to a compact axial-flow compressor stage. A central hub and spinner support a circular row of rotating blades, which increase the static pressure of the incoming air and accelerate it both axially and tangentially. This allows the air to be forced through the narrow passages developed by the cylinder fins, oil-cooler core, and cooling baffles [3], [4]. Too little pressure rise deprives the engine of cooling air, while an oversized fan wastes shaft power and makes noise. It is important to balance the pressure-flow characteristic of the fan with the pressure losses of this downstream ducting. The three-dimensional flow phenomena seen in a real cooling fan installation, such as tip-leakage vortices, hub-corner separation, blade-to-blade interaction, and secondary flow, are beyond the capabilities of classical blade-element and cascade design methods. As a result, computational fluid dynamics has replaced physical prototyping as the standard verification step [3]. In order to provide a validated geometric and computational baseline for future design refinement, this paper details a CATIA-to-CFD workflow for a representative sixteen-blade aircraft engine cooling fan. The model was created in CATIA V5, and then analyzed in ANSYS CFX under a fixed inlet-velocity boundary condition. The goal was to quantify the resulting pressure field, as well as the aerodynamic forces and moments that the fan develops.

## II. REVIEW OF LITERATURE

Air-cooled piston aero-engines are lighter, less mechanically complex, and easier to maintain than liquid-cooled ones. They dissipate heat directly to the atmosphere through finned cylinder barrels and heads. The effectiveness of this convective process is governed by factors such as fin geometry, spacing, material conductivity, and local airflow velocity [1], [4]. While ram-air cooling is sufficient at cruising speed, it becomes inadequate at ground and low speeds, which is why supplemental cooling fans operated by engines or electricity are used. This is especially true in rotorcraft, where the forward-speed cooling mechanism is eliminated during lengthy hover operation [2], [3]. When sizing fans, it's important to consider environmental factors that impair convective cooling performance, such as high temperatures, high altitude, and lower air density [3]. The theory of lift in turbomachinery is directly applicable to the aerodynamics of axial-flow fans. In this case, the relative flow between the axial inflow and the tangential velocity of the blades acts as a lift force generator, and the pressure increase is controlled by the equation developed by Euler in turbomachinery, which relates the change in angular momentum imparted to the fluid to the energy transfer [1]. Design parameters like blade chord, camber, thickness, aspect ratio, hub-to-tip ratio, and solidity (chord divided by spacing) govern the achievable pressure rise, efficiency, and installation envelope [1], [2]. Since tangential velocity increases with radius, blade stagger and twist must vary along the span to keep each section operating near its optimum angle of attack. Compared to a lower-solidity design, the fan under consideration here has a high-solidity, high-blade-count layout, which allows for a big pressure increase within a compact axial length but comes at the expense of profile loss, blade interference, and decreased peak efficiency [1], [2]. Among the aerodynamic loss processes unique to axial fans are the following: boundary-layer separation due to negative pressure gradients; pressure differential across the blade tip clearance driving vortices at the blade tips; and secondary flows created at the hub and casing endwalls [1, 3].

The present study followed the industry standard for creating fan, propeller, and compressor blade geometry using parametric, feature-based computer-aided design (CAD) systems like CATIA V5. This method involves drawing a single blade section, aligning it around the hub axis using a circular-pattern operation, and then combining the result with a hub/spinner solid of revolution [6]. Here, we use a simpler stationary-frame, fixed-inlet-velocity case to establish mesh quality, boundary-condition definition, and solver stability before running a full rotating-frame simulation. ANSYS CFX provides a coupled, implicit finite-volume solution of the Navier-Stokes equations, which is well-suited to internal and turbomachinery flows, as well as dedicated Frozen Rotor and Transient Rotor-Stator interface models for rotating-frame analysis. One common way to handle mesh density and topology differences between geometrically different parts of a rotor assembly is to split the fluid volume into multiple connected regions, such as a hub/spinner domain and an outer-flow domain, connected through a General Connection or General Grid Interface [7]. The standard method for determining whether a steady-state CFD solution has converged is to lower the RMS residuals to a predetermined value, usually $1 \times 10^{-4}$ for engineering-accuracy work, and to keep the normalized mass and momentum imbalance throughout the domain below around 1% [9]. This paper's focus is on a real-world scenario where the solution does not diverge but residuals plateau above the nominal target. This happens when the laminar model is applied to a physically turbulent flow or when there are local mesh-quality issues. In such cases, the use of the result is primarily determined by the imbalance criterion and the physical plausibility of the field. The current paper contributes to the literature by documenting a complete CATIA-to-CFX workflow for an aircraft engine cooling fan and by providing a transparent, quantitative discussion of a case where the nominal residual target is not fully met within the available iteration budget. While general CFD methodology for turbomachinery and axial-fan aerodynamics are well-established, there are few studies that specifically address this topic.

## III. STUDY DESIGN

**A.** Technical Details and Array of Blades

A sixteen-blade axial-flow rotor fan with high solidity is being studied. It has a conical-spinner/cylindrical-hub assembly and a row of blades that go around the circumference. Each blade is designed with a unique profile and arranged at an equal angle spacing of 22.5° (360°/16) utilizing the Circular Pattern feature. Table I provides a brief overview of the study's primary design and flow parameters. The choice of a relatively high blade count is in line with the norm for small, high-pressure-rise engine cooling fans that have to fit into a constrained cowling. However, this comes at the expense of reduced peak efficiency, increased surface friction, and loss due to blade interference, as well as increased solidity and the amount of pressure that can be raised per stage at a given tip speed.

The Design of Cooling Fans and Their Flow Parameters (Table I)

| Parameter | Value / Description |
|---|---|
| Fan type | Axial-flow, engine-driven cooling fan |
| Number of blades | 16 |
| Hub / spinner type | Conical nose spinner with cylindrical hub |
| Blade planform | Flat, radially arrayed rectangular/tapered blade |
| Fluid domain topology | Two connected regions: inner hub/spinner domain + outer blade/flow domain |
| Working fluid | Air ($\rho = 1.184$ kg/m³, $\mu = 1.849 \times 10^{-5}$ Pa·s) |
| Inlet condition | Uniform normal velocity = 65 m/s |
| Outlet condition | Average static pressure = 0 Pa (gauge) |
| Modelling software | CATIA V5 (Sketcher, Part Design, Assembly Design) |
| CFD software | ANSYS Workbench 19.5 — Fluid Flow (CFX) |

**B.** CATIA V5: Simulation of Solids

Using CATIA's Sketcher, Part Design, Wireframe, and Surface Design workbenches, the whole fan geometry was created as a single part. A conical/ogive nose section and a cylindrical hub section were combined in the design of the spinner. The hub section was sized to accommodate the blade roots and the accessory drive-shaft mounting bore. The result is a smooth aerodynamic profile that directs incoming air into the blade-swept annulus and minimizes flow disturbance at the fan centerline. Then, using a radial reference plane, we defined the chord length, thickness, leading/trailing-edge geometry, and stagger angle for a single blade profile. Then, we extruded this profile into a solid blade feature, using root fillets to mitigate local stress concentration and smooth the transition into the hub. Applying the Circular Pattern feature to this one blade feature resulted in sixteen evenly spaced instances being generated in a single parametric operation. This ensured perfect rotational symmetry and made it possible to adjust one feature instead of sixteen to change the blade count or stagger angle. Blade stagger, spinner-fairing continuity, and root-fillet geometry were checked using front, isometric, and back views of the final assembly. Standard orthographic views were created in the Drafting workbench before the part was exported for CFD analysis.

**C.** Problems with the Fluid Domain, Mesh, and Boundaries

To account for the disparity in local geometric complexity between the smaller spinner/hub region and the larger blade-swept flow field, the imported fan geometry was contained within two interconnected fluid regions: one was a smaller inner Default Domain that encased the spinner and hub, and the other was a larger outer fluid domain that encased the blades and the surrounding inlet, outlet, and outer-wall flow fields. Using a conservative interface-flux formulation, the two domains were linked via a fluid-fluid General Connection interface. Both domains were solved in a stationary reference frame. This two-domain method maintained a completely linked, conservative solution throughout the assembly, allowing for separate meshing of the basic hub geometry and the aerodynamically crucial blade regions. The coarser mesh covered the former, while the much finer mesh covered the latter. We used an unstructured, all-tetrahedral element method in ANSYS Meshing to discretize each area. Table II provides a concise summary of the results for both the individual domain meshes and the combined global mesh.

The table I. Fluid Domain-Based Mesh Statistics

| Mesh Statistic | Value |
|---|---|
| Default Domain — Nodes | 163 |
| Default Domain — Elements (tetrahedra) | 525 |
| Default Domain — Faces | 228 |
| Fluid domain — Nodes | 25,000 |
| Fluid domain — Elements (tetrahedra) | 132,809 |
| Fluid domain — Faces | 12,014 |
| Global — Total nodes | 25,163 |
| Global — Total elements (tetrahedra) | 133,334 |

All elements in the tiny Default Domain met acceptable orthogonal-angle and expansion-factor limits, indicating satisfactory mesh quality throughout. The majority of the mesh still met the quality thresholds, and the marginal cells are identified as a specific target for local refinement in future work, such as boundary-layer inflation and finer trailing-edge sizing. Still, a small fraction of elements in the larger fluid domain were flagged as marginal, with less than 1% by orthogonal angle and about 1% by expansion factor. These elements were likely concentrated at the thin trailing edges and root fillets of the sixteen closely spaced blades. Under an isothermal, non-buoyant, laminar flow model and a steady-state analysis type, air was designated as the working fluid. Its density is 1.184 kg/m³ and its dynamic viscosity is $1.849 \times 10^{-5}$ Pa·s. The CFX solver was run with a High Resolution advection scheme, automatic timescale control, a maximum of 100 outer-loop iterations, and an RMS residual convergence target of $1 \times 10^{-4}$. The parameters included an average static-pressure outlet, a uniform normal inlet velocity of 65 m/s, and no-slip conditions on the surfaces of the blade, hub, and duct-wall.

## IV. THE OUTCOME

At the simulated 65 m/s intake condition, this section depicts the solution's convergence behavior, the resulting pressure and velocity fields, and the aerodynamic forces and moments acting on the fan.

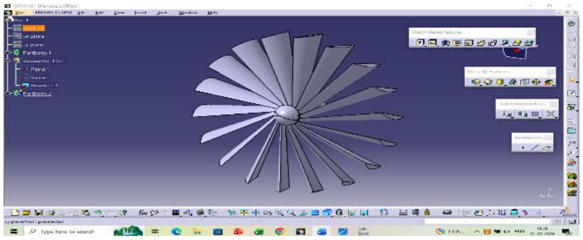

Fig 1. The two-domain fluid model in ANSYS Designer / SpaceClaim shows the inlet, outlet, and interface faces, as well as the inner hub/ spinner domain and the outside blade/flow domain.

**A.** The Behavior of Convergence and Mesh-Imbalance

After 132 seconds of wall-clock solution time, the solver was run to the maximum 100-iteration budget, however it failed to attain the nominal RMS residual objective of $1 \times 10^{-4}$. The final residuals for the momentum and mass equations are shown in Table III.

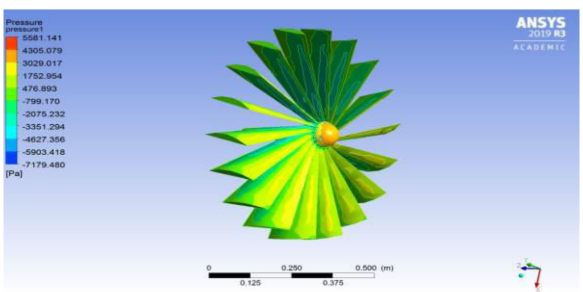


Fig 2. Dynamic pressure profile on the spinner and blades of the engine's cooling fan

TABLE III. Real Mean Squared Deviations from the Convergence Objective

| Equation | Final RMS Residual | Target | Status |
|---|---|---|---|
| U-Momentum | $8.0 \times 10^{-4}$ | $1 \times 10^{-4}$ | Above target |
| V-Momentum | $9.8 \times 10^{-4}$ | $1 \times 10^{-4}$ | Above target |
| W-Momentum | $2.6 \times 10^{-3}$ | $1 \times 10^{-4}$ | Above target |
| P-Mass | $1.7 \times 10^{-4}$ | $1 \times 10^{-4}$ | Marginally above target |

Looking at the residual trend in the last iterations revealed a very gradual rise instead of divergence, suggesting a quasi-steady plateau instead of a monotonically converging solution. Therefore, just increasing the iteration count wouldn't have automatically lowered the residuals to the goal. Regardless, as shown in Table IV, the normalized mass and momentum imbalance summary, conservation in both domains was found to be well within engineering-acceptable bounds, with all equations falling below ±0.04%, which is far tighter than the usually accepted ±1% engineering standard.

TABLE IV. Imbalance of Normalized Mass and Momentum at the Last Iteration

| Equation / Domain | Imbalance (%) |
|---|---|
| U-Momentum — Default Domain | 0.0000 |
| V-Momentum — Default Domain | 0.0001 |
| W-Momentum — Default Domain | 0.0002 |
| P-Mass — Default Domain | −0.0004 |
| U-Momentum — fluid domain | −0.0372 |
| V-Momentum — fluid domain | −0.0024 |
| W-Momentum — fluid domain | 0.0090 |

For preliminary aerodynamic evaluation, this combination of plateaued residuals and extremely low imbalance suggests a mass- and momentum-conservative solution; nevertheless, local flow details should be taken with care, as will be detailed in Section V.

**B.** Acceleration and Deceleration System

When it comes time for the last iteration, Table V summarizes the lowest and greatest values of the primary flow variables in each domain. Because of the intense local acceleration and pressure gradients produced at the surfaces of the spinning blades, the fluid domain's pressure and velocity range is much greater than that of the Default Domain. This is in contrast to the spinner/hub area, where the field is relatively mild and homogeneous.

Table V. Domain-Specific Variable Ranges

| Variable | Minimum | Maximum |
|---|---|---|
| Velocity u — Default Domain | −49.4 m/s | 54.0 m/s |
| Velocity v — Default Domain | −43.7 m/s | 54.4 m/s |
| Velocity w — Default Domain | −7.69 m/s | 49.4 m/s |
| Static pressure — Default Domain | $2.65 \times 10^3$ Pa | $4.80 \times 10^3$ Pa |
| Velocity u — fluid domain | −50.9 m/s | 62.7 m/s |
| Velocity v — fluid domain | −49.5 m/s | 57.4 m/s |
| Velocity w — fluid domain | −67.0 m/s | 110 m/s |
| Static pressure — fluid domain | $-7.18 \times 10^3$ Pa | $5.58 \times 10^3$ Pa |

There was a noticeable difference in the static-pressure contour on the spinner and blade surfaces. On the pressure side, which faced upstream, the contour reached positive gauge values up to about 5.58 kPa. On the suction side and blade-tip regions, however, the local static pressure dropped to negative gauge values as low as about −7.18 kPa. This difference across all sixteen blades is the direct mechanism by which the fan achieves static pressure rise and axial airflow. Since the fan geometry and boundary conditions are axisymmetric, the pressure field was likely due to local mesh-quality variation and incomplete residual convergence, as discussed in Section IV-A, rather than genuine physical asymmetry. The pressure field was non-uniform both radially and from blade to blade, with the former increasing toward the blade tips, where the relative and tangential velocities were highest, and the latter from blade to blade.

**C.** What Follows: Moments and Forces

Table VI summarizes the components of the pressure, viscous force, and moment acting on the blade/spinner, outer-wall, and fluid-fluid interface surfaces, as integrated by the solver during the last iteration. These loads are important for the structural design of the fan drive and for the following shaft-torque calculations because they reflect the net aerodynamic loading and thrust that the fan produces at the simulated intake condition.

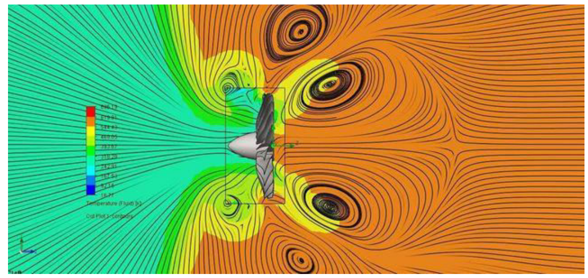

Figure 3. displays the outcomes of the plot experiment.

| Quantity | Component | Value |
|---|---|---|
| Pressure force | X | 17.48 N |
| Pressure force | Y | 11.53 N |
| Pressure force | Z (axial) | 475.64 N |
| Viscous force | X | $-2.96 \times 10^{-4}$ N |
| Viscous force | Y | $1.41 \times 10^{-3}$ N |
| Viscous force | Z | 0.163 N |
| Pressure moment | X | 2.43 N·m |
| Pressure moment | Y | 0.623 N·m |
| Pressure moment | Z (axial) | −143.45 N·m |
| Viscous moment | X | $7.72 \times 10^{-4}$ N·m |
| Viscous moment | Y | $-3.59 \times 10^{-4}$ N·m |
| Viscous moment | Z | $5.56 \times 10^{-3}$ N·m |

The net axial thrust and pressure rise delivered by this bluff, high-solidity rotor are governed by pressure (form) forces, with viscous skin-friction forces being relatively negligible. The dominant load component is the axial (Z-axis) pressure force, which is over three orders of magnitude larger than the corresponding viscous force component, at 476 N. In order to spin the fan against the flow, the drive shaft must overcome an aerodynamic torque, which is physically represented by the axial pressure moment of around -143.5 N·m. This moment directly influences the size of the fan drive shaft, bearings, and connection.

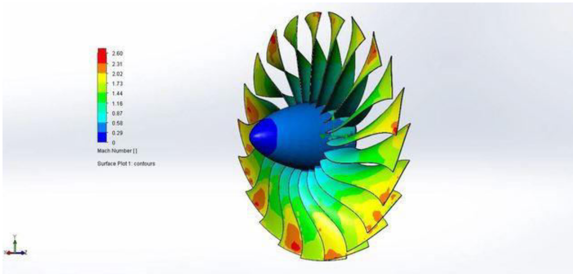


Fig 4. Coverage diagram

## V. THEME DEBATE

Before incorporating these findings into your design, you should consider three key components of the current study. The 100-iteration solver budget did not allow the RMS residuals to drop below the nominal $1 \times 10^{-4}$ target. Despite the conservative solution overall, the incompletely converged residuals suggest that local flow details, especially the variation in blade-to-blade pressure noted in Section IV-B, should be handled with care. The reported magnitudes of pressure-rise and force are more accurately seen as indicative than final design values. Rather than active divergence, the residual trend during the last iterations indicated a quasi-steady plateau, suggesting that increasing the iteration count alone would not be enough to achieve complete convergence unless mesh quality is also addressed or the solver timescale factor is reduced. Secondly, about one percent of the elements in the bigger fluid domain were marked as having poor orthogonal-angle and marginal expansion-factor quality. This is likely concentrated at the thin trailing edges of the blades and root fillets. These local mesh deficiencies can reduce the accuracy of the solutions in the areas where the aerodynamics are most important, which could explain the residual plateau. Thirdly, the laminar flow model is not applicable to flows with an effective Reynolds number of around $2.4 \times 10^5$ in the Default Domain. A bluff, high-solidity rotating blade row at this Reynolds number would show turbulent boundary-layer behavior, separation, and wake mixing, which the model cannot capture. Therefore, the most important thing to improve for future work is to find an appropriate turbulence closure, such as SST k-ϋ. Although the mesh, boundary-condition, and solution methodology utilized here are directly extensible to a rotating-frame simulation at a specified fan RPM using a Frozen Rotor or Transient Rotor-Stator interface, the current formulation does not account for the Coriolis and centrifugal effects inherent to a real rotating fan because it uses a stationary reference frame at a fixed inlet velocity that represents the fan's mean discharge condition instead. These limitations should be considered as an initial baseline for validating geometry and workflow rather than a representation of certification performance, but they do not affect the overall physical plausibility of the pressure-rise and force results obtained.

## VI. CONCLUSION

After creating a comprehensive three-dimensional solid model in CATIA V5, the model was imported into ANSYS Workbench. Inside ANSYS, the model was contained within a two-region fluid domain and discretized into a combined tetrahedral mesh with 25,163 nodes and 133,334 elements. The fan, which has sixteen blades, is designed to cool an axial engine. Using air as the working fluid, an inlet velocity of 65 m/s, an average static pressure outlet, and no-slip walls, a full 100-iteration budget for a steady-state CFX simulation was solved. Although the nominal RMS residual target of $1 \times 10^{-4}$ was not reached, the final residuals ranged from approximately $1.7 \times 10^{-4}$ to $2.6 \times 10^{-3}$. Normalized mass and momentum imbalances stayed below 0.04% for every equation, indicating a conservative solution that is usable for preliminary assessment. A static-pressure differential across the fan ranging from about -7.18 kPa to +5.58 kPa was observed in the resultant flow field, with local velocities reaching 110 m/s close to the blade tips. This aligns with the anticipated pressure-rise mechanism of an axial cooling fan. The dominant axial pressure force was about 476 N, and the corresponding axial pressure moment was about -143.5 N·m, which is more than three orders of magnitude larger than the viscous force and moment components. These figures directly measure the thrust and shaft-torque requirements of the cooling-fan drive. Rather than ignoring specific mesh-quality and convergence limitations, as well as the laminar-flow and stationary-frame simplifications, these were identified and quantified. Moving forward, we have concrete recommendations to improve the accuracy of future analyses of this cooling-fan geometry, such as a rotating-reference-frame formulation, an appropriate turbulence closure, an extended iteration count with local mesh refinement, a formal grid-independence study, and bench-test validation.

## REFERENCES

[1] S. L. Dixon and C. A. Hall, Fluid Mechanics and Thermodynamics of Turbomachinery, 7th ed. Oxford, U.K.: Butterworth-Heinemann, 2014.

[2] R. A. Wallis, Axial Flow Fans and Ducts. New York, NY: John Wiley & Sons, 1983.

[3] F. P. Bleier, Fan Handbook: Selection, Application, and Design. New York, NY: McGraw-Hill, 1997.

[4] M. J. Kroes and T. W. Wild, Aircraft Powerplants, 8th ed. New York, NY: McGraw-Hill Education, 2014.

[5] Federal Aviation Administration, Aviation Maintenance Technician Handbook — Powerplant, FAA-H-8083-32. Washington, DC: U.S. Dept. of Transportation, 2018.

[6] Dassault Systèmes, CATIA V5 Part Design User's Guide. Vélizy-Villacoublay, France: Dassault Systèmes.

[7] ANSYS, Inc., ANSYS CFX-Solver Modeling Guide, Release 19.5. Canonsburg, PA: ANSYS, Inc., 2019.

[8] ANSYS, Inc., ANSYS CFX-Solver Theory Guide, Release 19.5. Canonsburg, PA: ANSYS, Inc., 2019.

[9] H. K. Versteeg and W. Malalasekera, An Introduction to Computational Fluid Dynamics: The Finite Volume Method, 2nd ed. Harlow, U.K.: Pearson Education, 2007.

[10] J. D. Anderson Jr., Fundamentals of Aerodynamics, 6th ed. New York, NY: McGraw-Hill Education, 2017.

[11] D. Japikse and N. C. Baines, Introduction to Turbomachinery. Oxford, U.K.: Concepts ETI / Oxford University Press, 1997.

[12] P. J. Roache, "Perspective: a method for uniform reporting of grid refinement studies," J. Fluids Eng., vol. 116, no. 3, pp. 405–413, 1994.